

76

SATELLITE & MESOMETEOROLOGY RESEARCH PROJECT

Department of the Geophysical Sciences
The University of Chicago

A MODEL OF TYPHOONS WITH OUTFLOW AND SUBSIDENCE LAYERS

by

Tatsuo Izawa

SMRP Research Paper

Number 76

January 1969



MESOMETEOROLOGY PROJECT --- RESEARCH PAPERS

- 1.* Report on the Chicago Tornado of March 4, 1961 - Rodger A. Brown and Tetsuya Fujita
- 2.* Index to the Nssp Surface Network - Tetsuya Fujita
- 3.* Outline of a Technique for Precise Rectification of Satellite Cloud Photographs - Tetsuya Fujita
- 4.* Horizontal Structure of Mountain Winds - Henry A. Brown
- 5.* An Investigation of Developmental Processes of the Wake Depression Through Excess Pressure Analysis of Nocturnal Showers - Joseph L. Goldman
- 6.* Precipitation in the 1960 Flagstaff Mesometeorological Network - Kenneth A. Styber
- 7.** On a Method of Single- and Dual-Image Photogrammetry of Panoramic Aerial Photographs - Tetsuya Fujita
8. A Review of Researches on Analytical Mesometeorology - Tetsuya Fujita
- 9.* Meteorological Interpretations of Convective Neph systems Appearing in TIROS Cloud Photographs - Tetsuya Fujita, Toshimitsu Ushijima, William A. Hass, and George T. Dellert, Jr.
- 10.* Study of the Development of Prefrontal Squall-Systems Using Nssp Network Data - Joseph L. Goldman
11. Analysis of Selected Aircraft Data from Nssp Operation, 1962 - Tetsuya Fujita
12. Study of a Long Condensation Trail Photographed by TIROS I - Toshimitsu Ushijima
13. A Technique for Precise Analysis of Satellite Data; Volume I - Photogrammetry (Published as MSL Report No. 14) - Tetsuya Fujita
14. Investigation of a Summer Jet Stream Using TIROS and Aerological Data - Kozo Ninomiya
15. Outline of a Theory and Examples for Precise Analysis of Satellite Radiation Data - Tetsuya Fujita
16. Preliminary Result of Analysis of the Cumulonimbus Cloud of April 21, 1961 - Tetsuya Fujita and James Arnold
17. A Technique for Precise Analysis of Satellite Photographs - Tetsuya Fujita
- 18.* Evaluation of Limb Darkening from TIROS III Radiation Data - S.H.H. Larsen, Tetsuya Fujita, and W.L. Fletcher
19. Synoptic Interpretation of TIROS III Measurements of Infrared Radiation - Finn Pedersen and Tetsuya Fujita
- 20.* TIROS III Measurements of Terrestrial Radiation and Reflected and Scattered Solar Radiation - S.H.H. Larsen, Tetsuya Fujita, and W.L. Fletcher
21. On the Low-level Structure of a Squall Line - Henry A. Brown
- 22.* Thunderstorms and the Low-level Jet - William D. Bonner
- 23.* The Mesoanalysis of an Organized Convective System - Henry A. Brown
24. Preliminary Radar and Photogrammetric Study of the Illinois Tornadoes of April 17 and 22, 1963 - Joseph L. Goldman and Tetsuya Fujita
25. Use of TIROS Pictures for Studies of the Internal Structure of Tropical Storms - Tetsuya Fujita with Rectified Pictures from TIROS I Orbit 125, R/O 128 - Toshimitsu Ushijima
26. An Experiment in the Determination of Geostrophic and Isalobaric Winds from Nssp Pressure Data - William Bonner
27. Proposed Mechanism of Hook Echo Formation - Tetsuya Fujita with a Preliminary Mesosynoptic Analysis of Tornado Cyclone Case of May 26, 1963 - Tetsuya Fujita and Robbi Stuhmer
28. The Decaying Stage of Hurricane Anna of July 1961 as Portrayed by TIROS Cloud Photographs and Infrared Radiation from the Top of the Storm - Tetsuya Fujita and James Arnold
29. A Technique for Precise Analysis of Satellite Data, Volume II - Radiation Analysis, Section 6. Fixed-Position Scanning - Tetsuya Fujita
30. Evaluation of Errors in the Graphical Rectification of Satellite Photographs - Tetsuya Fujita
31. Tables of Scan Nadir and Horizontal Angles - William D. Bonner
32. A Simplified Grid Technique for Determining Scan Lines Generated by the TIROS Scanning Radiometer - James E. Arnold
33. A Study of Cumulus Clouds over the Flagstaff Research Network with the Use of U-2 Photographs - Dorothy L. Bradbury and Tetsuya Fujita
34. The Scanning Printer and Its Application to Detailed Analysis of Satellite Radiation Data - Tetsuya Fujita
35. Synoptic Study of Cold Air Outbreak over the Mediterranean using Satellite Photographs and Radiation Data - Aasmund Rabbe and Tetsuya Fujita
36. Accurate Calibration of Doppler Winds for their use in the Computation of Mesoscale Wind Fields - Tetsuya Fujita
37. Proposed Operation of Instrumented Aircraft for Research on Moisture Fronts and Wake Depressions - Tetsuya Fujita and Dorothy L. Bradbury
38. Statistical and Kinematical Properties of the Low-level Jet Stream - William D. Bonner
39. The Illinois Tornadoes of 17 and 22 April 1963 - Joseph L. Goldman
40. Resolution of the Nimbus High Resolution Infrared Radiometer - Tetsuya Fujita and William R. Bandeen
41. On the Determination of the Exchange Coefficients in Convective Clouds - Rodger A. Brown

* Out of Print

** To be published

(Continued on back cover)

SATELLITE AND MESOMETEOROLOGY RESEARCH PROJECT

Department of the Geophysical Sciences

The University of Chicago

A MODEL OF TYPHOONS WITH OUTFLOW AND SUBSIDENCE LAYERS

by

Tatsuô Izawa

The University of Chicago

and

Meteorological Research Institute, Tokyo

SMRP Research Paper No. 76



January 1969

The research reported in this paper was sponsored by US ESSA under Grant CWB-E-22-45-68-(G).

A MODEL OF TYPHOONS WITH OUTFLOW AND SUBSIDENCE LAYERS¹

by

Tatsuo Izawa
The University of Chicago
and
Meteorological Research Institute, Tokyo

ABSTRACT

The Nimbus and ESSA pictures of hurricanes and typhoons reveal that longitudinal bands of convective clouds appear outside a relatively clear annular zone around the storm and these longitudinal bands at times are accompanied by well-defined transverse bands which are characterized by mesoscale cloud streaks.

In order to generalize the model of typhoons accompanied by inner and outer rainbands by Fujita, Izawa, et al. (1967), a modified model of typhoons was proposed. In this model, a subsidence layer was added to the original outflow layer in order to permit the air to descend from the outflow to the subsidence layer. The model also permits the air in the subsidence layer to ascend to the outflow layer by entraining the air into the updraft. The middle layer of the previous model was also used to transport the absolute angular momentum inside the radar echoes through the subsidence layer to the outflow layer.

One of the most interesting results obtained from the present model is the relation between the orientation of the outflow cirrus bands and the vertical wind shear. The computed wind shear between the outflow and the middle layers coincides with the general pattern of wide longitudinal bands of cirrus clouds, while the transverse bands which are nearly perpendicular to the general orientation of the longitudinal bands were found to represent the computed wind shear between the outflow and the subsidence layer.

¹The research reported in this paper was sponsored by US ESSA under Grant CWB-E-22-45-68-(G).

1. Introduction

The TIROS meteorological satellites dating back to April 1960 have brought us a great deal of new knowledge on hurricanes and typhoons. Fett (1964) found that TIROS hurricane and typhoon pictures reveal at least two major features which appear to characterize many tropical storms: (1) a relatively clear annular zone of subsidence appears, curving around the periphery of the high cloud shield of a tropical storm and (2) outer convective bands often appear, exterior to the annular zone. These bands at times develop to full squall line intensity.

The High Resolution Infrared Radiometer (HRIR) carried by the Nimbus I meteorological satellite launched in August 1964 provided detailed depiction of cloud features of hurricanes on the dark side of the earth. Allison, et al. (1966) analyzed the Nimbus I pictures of Hurricanes Gladys and Dora, showing the existence of an annular zone of subsidence and outer convective bands.

Typhoon Bess of 1963 discussed by Fujita, Izawa et al. (1967) was accompanied by well-defined inner and outer rainbands. From the detailed analysis of TIROS and radar pictures and other conventional meteorological data, it was found that the clouds near the typhoon center appear as the "inner cirrus shield" covering mostly the region of inner rainbands, and the "outer cirrus decks" are seen over the outer rainbands which propagate outward, leaving an annular ring of relatively clear sky. Numerical experiments with a two-layer model indicated that the vertical transport of angular momentum by outer rainbands alters the outflow pattern, resulting in the formation of a ring of high cloud-free region which separates the inner cirrus shield from the outer cirrus decks.

The banded structure of convection in the atmosphere has been studied by many authors. It is well known that convection in the atmosphere takes place in the form of Benard cells when the vertical wind shear within the convective layers is small. With increasing shear the tilt of these cell axes is so large that the cellular convection gradually changes into transverse rolls, commonly observed under moderate wind shear. An experimental study made by Chandra (1938) revealed the transitions from open cells to transverse rolls and finally to longitudinal bands when the vertical wind shear was increased. On the other hand, from his dynamical consideration, Kuettner (1959) showed that the banded structure of clouds as seen in the trade winds, tropical cyclones, and many other phenomena in the atmosphere

is more closely related to the wind shear gradient than to the wind shear. This dynamical approach would be more attractive than purely kinematical considerations such as the deformation of the pre-existing convective cells in shear flows. According to his estimate, the required wind shear gradient is $10^{-7} \text{cm}^{-1} \text{sec}^{-1}$.

Tsuchiya and Fujita, however, (1967) showed that convective clouds which form over the western Pacific under the influence of the Winter Monsoon are more closely related to the wind shear than to the wind shear gradient. According to their study, the top of these convective clouds is as low as about the 700 mb level, and the convective regimes are represented by longitudinal bands when wind shear is strong, transverse bands when wind shear is moderate, and cellular clouds when wind shear is weak.

On the other hand, clouds surrounding hurricanes or typhoons are so high as to reach about the 200 mb level where outflow winds are blowing with a difference of about 180 deg between the directions of this high level and the surface winds. The Nimbus and ESSA pictures of hurricane or typhoon clouds reveal that longitudinal bands of outer convective clouds are very often accompanied by well-defined transverse bands which are nearly perpendicular to the general orientation of these longitudinal bands. The direction of longitudinal and transverse bands of clouds would be more closely related to wind shears between higher levels than to those between lower levels.

In the present paper, by using a typhoon model with outflow and subsidence layers, it will be shown that the general orientation of the longitudinal bands coincides with the computed wind shear between the outflow and middle layers, while the direction of the transverse bands coincides with the computed wind shears between the outflow and subsidence layers. Since the present model permits the air in the subsidence layer to entrain into the updraft, the effect of entrainment upon the outflow winds will also be discussed.

2. Longitudinal and Transverse Bands in Clouds Seen in Satellite Pictures

Typhoon Bess of 1963 discussed by Fujita, Izawa, et al. (1967) revealed that a well-defined eye of about 50 km in diameter is clearly seen and relatively thick cirrostratus covers the inner portion of the storm while the outer portion is characterized by locally thick cirrus clouds which are closely related to the distribution of convective cells forming the outer rainbands.

The aim of this section is to present some other examples of longitudinal and transverse bands in hurricane and typhoon clouds seen in the Nimbus and ESSA satellite pictures. Figure 1 shows an HRIR photofacsimile depiction of Hurricane Gladys taken on Orbit 305, at 0422 U. T., 18 September 1964. On this particular orbit the spacecraft passed directly over the eye of Gladys, where the response of the radiometer was the highest in the analog trace (Allison, et al., 1966). To the west and north of Gladys may be seen a relatively cloud-free region between the hurricane and the longitudinal band of outer convective clouds, and the transverse bands may also be seen, characterized by mesoscale cloud streaks which are almost perpendicular to the general orientation of these longitudinal bands.

Figure 2 shows another HRIR photofacsimile depiction of Hurricane Dora, taken on Orbit 174, at 0530 U. T., 9 September 1964. The eye of Dora was about 90 miles east of Daytona Beach, Florida at the time of the satellite pass (Allison, et al., 1966). In the northwest quadrant of Dora, there are several longitudinal bands of cloudiness accompanied by transverse bands which are almost perpendicular to these outer bands. Beyond the outermost band of cloudiness was found peripheral subsidence associated with the hurricane outflow (Reap, 1966).

Presented in Fig. 3 is an ESSA-2 APT picture of typhoon Opal taken on Orbit 7052, at 2228Z, 8 September 1967. On this particular day the storm was centered at about 27N, 147E and reached the minimum central pressure of 958 mb. Typhoon Opal moved north-northwest and then veered to northeast without landing on the Japan Islands. Around the typhoon there are several longitudinal bands of outer cloudiness accompanied by transverse bands which are nearly perpendicular to these outer bands.

Figure 4 shows a Nimbus 2 APT picture of typhoon Amy taken on Orbit 6747, at 0153Z, 4 October 1967. On this particular day the storm was centered at about 24N, 148.5E, and reached the central pressure of 970 mb. Because of the large zenith angle of the sun at the time of the satellite pass and a low contrast between black and white colors in the picture recorded on facsimile paper, no detail of cloud feature near the eye of the storm could be provided. To the east of the storm, however, may be seen well-defined transverse bands which are nearly perpendicular to the outer longitudinal band. ®

Also presented in Fig. 5 is an ESSA-6 APT picture of typhoon Mary taken on Orbit 3212, at 0018Z, 24 July 1968. On this particular day the storm was centered at about 21N,

153E, and reached the minimum central pressure of 925 mb. To the northeast of the storm may be seen a sunglint spot. Because of the large zenith angle of the sun at the time of the satellite pass, there may be seen ill-defined shadows of inner cirrus bands on the picture. To the west of the storm, however, may be seen transverse bands which are nearly perpendicular to longitudinal bands of outer cloudiness.

In the present paper it will be shown that the direction of longitudinal and transverse bands as seen in these satellite pictures of hurricanes and typhoons are closely related to the vertical wind shears between upper levels rather than those between lower levels.

3. A Proposed Model with Outflow and Subsidence Layers

The physical and mathematical basis of the present model as well as the previous model of typhoon outflow lies in the principles of conservation of mass and absolute angular momentum.

Figure 6 shows a schematic model of a typhoon with outflow and subsidence layers. At the top of the outflow layer a solid boundary is taken all the way out through which the air is not permitted to pass. For the region of downdraft, the same boundary condition is also assumed at the bottom of the subsidence layer so that the air can descend only through the boundary between the layers. For the region of updraft, however, an open boundary is taken at the bottom of the subsidence layer so that the air can ascend all the way from the middle layer to the outflow layer with entrainment of air in the subsidence layer. For the convenience of later discussion we shall define the suffix i which refers to the quantity at the outflow layer when $i=1$ and to that at the subsidence layer when $i=2$.

Equation of Continuity

Presented in Fig. 7 is the mass flux diagram for downdraft and updraft. The radial mass flux across the cylindrical surfaces with constant thickness h_i at radius r is given by $2\pi r h_i u_i$, respectively. Since the radial velocity u_i is changed into $u_i + du_i$, while the air is passing over the distance between r and $r + dr$, the radial mass flux across the cylindrical surface at radius $r + dr$ is expressed by $2\pi h_i (r + dr)(u_i + du_i)$, respectively. For the vertical mass flux, different expressions are given between the region of downdraft and updraft.

For the region of downdraft we simply assume that the vertical mass flux across the boundary between the outflow and the subsidence layers is given by $2\pi r w dr$. Thus by the conservation of mass we have for the equations of continuity

$$\frac{1}{r} \frac{d}{dr} (r u_1) + \frac{w}{h_1} = 0 \quad (1)$$

and

$$\frac{1}{r} \frac{d}{dr} (r u_2) - \frac{w}{h_2} = 0 \quad (2)$$

when $w < 0$. From Eqs. (1) and (2), we obtain the relation

$$\frac{d}{dr} (h_1 r u_1 + h_2 r u_2) = 0 \quad (3)$$

This means that the total radial mass flux across the layers with thickness h_1 and h_2 remains unchanged while the air is flowing over the region of downdraft.

For the region of updraft there is a vertical mass flux through the bottom of the subsidence layer which is given by $2\pi r w dr$. This air is also assumed to be able to ascend through the boundary between the layers to the outflow layer, with entrainment of the air in the subsidence layer. Thus the vertical mass flux through the boundary between the layers is given by $2\pi r (1 + E h_1) w dr$, where E is the entrainment rate defined by $E = \partial w / w \partial h$. By the conservation of mass we have for the equation of continuity

$$\frac{1}{r} \frac{d}{dr} (r u_1) + \frac{E h_1 w}{h_1} = 0 \quad (4)$$

and

$$\frac{1}{r} \frac{d}{dr} (r u_2) - \frac{(1 + E h_1) w}{h_2} = 0 \quad (5)$$

when $w > 0$. From Eqs. (4) and (5) we have

$$\frac{d}{dr} (h_1 r u_1 + h_2 r u_2) = r w \quad (6)$$

It is seen that the total radial mass flux across the layers with thickness h_1 and h_2 is increased by receiving additional mass supplied through the bottom of the subsidence layer while the outflowing air is passing over the region of updraft. Equations (3) and (6) are used

to obtain the radial velocities for the outflow layer after the radial velocities for the subsidence layer were obtained from Eqs. (1) and (4).

Equations of Absolute Angular Momentum

The absolute angular momentum at the outflow and the subsidence layers is defined as

$$M_i = rv_i + \frac{1}{2} fr^2$$

where v_i is the tangential velocity and f is the Coriolis parameter. Similar to the radial mass flux, the radial flux of absolute angular momentum across the cylindrical surfaces with constant thickness h_i at radius r is given by $2\pi h_i r u_i M_i$. In this case, since the radial velocity u_i and the absolute angular momentum M_i are changed into $u_i + du_i$ and $M_i + dM_i$, while the air is passing over the distance between radii r and $r + dr$, the absolute angular momentum flux at radius $r + dr$ is expressed by $2\pi h_i (r + dr)(u_i + du_i)(M_i + dM_i)$. Also, similar to the vertical mass flux, the vertical flux of absolute angular momentum takes a different expression between the regions of downdraft and updraft.

For the region of downdraft, the vertical flux of absolute angular momentum through the boundary between the outflow and the subsidence layers is given by $2\pi r M_2 w dr$. Thus by the conservation of absolute angular momentum we obtain

$$\frac{1}{r} \frac{d}{dr} (r u_1 M_1) + \frac{1}{h_1} M_2 w = 0 \quad (7)$$

and

$$\frac{1}{r} \frac{d}{dr} (r u_2 M_2) - \frac{1}{h_2} M_2 w = 0 \quad (8)$$

when $w < 0$. By using the equation of continuity, Eq. (2), Eq. (8) can be reduced to

$$\frac{dM_2}{dr} = 0 \quad (9)$$

This means that the absolute angular momentum in the outflow layer is constant while the air is passing over the region of downdraft. From Eqs. (7) and (8), we obtain

$$\frac{d}{dr} (h_1 r u_1 M_1 + h_2 r u_2 M_2) = 0 \quad (10)$$

We observe that the total radial flux of absolute angular momentum across the layers with thickness h_1 and h_2 remains constant, while the air is passing over the region of down-draft.

For the region of updraft, the vertical flux of absolute angular momentum through the bottom of the subsidence layer is given by $2\pi r m w dr$, where m is the absolute angular momentum of radar echoes. Since the air inside the updraft ascends to the outflow layer with entrainment of the air in the subsidence layer, the vertical flux of absolute angular momentum through the boundary between the layers is expressed by $2\pi r(m + E h_1 M_1) w dr$, where E is the entrainment rate defined above. By the conservation of absolute angular momentum we have for the equations of absolute angular momentum

$$\frac{1}{r} \frac{d}{dr} (r u_1 M_1) + \frac{1}{h_1} E h_1 M_1 w = 0 \quad (11)$$

and

$$\frac{1}{r} \frac{d}{dr} (r u_2 M_2) - \frac{1}{h_2} (m + E h_1 M_1) w = 0 \quad (12)$$

when $w > 0$. By using the equation of continuity, Eq. (1), Eq. (12) is reduced to

$$\frac{dM_1}{dr} = 0, \quad (13)$$

showing that the absolute angular momentum in the subsidence layer is constant, while the air is passing over the region of updraft. From Eqs. (11) and (12) we obtain

$$\frac{d}{dr} (h_1 r u_1 M_1 + h_2 r u_2 M_2) = m w r \quad (14)$$

This means that the total radial flux of absolute angular momentum across the layers with the thickness h_1 and h_2 is increased by receiving additional absolute angular momentum of radar echoes supplied through the bottom of the subsidence layer while the air is passing over the region of updraft. Equations (10) and (14) are used to obtain the absolute angular momentum for the outflow layer after the absolute angular momentum for the subsidence layer was obtained from Eqs. (7) and (11).

4. Solutions of Equations

From the above discussion the equations of continuity to be solved are written as

$$\left. \begin{aligned} \frac{d}{dr}(ru_1) &= -Ewr \\ \frac{d}{dr}(h_1ru_1 + h_2ru_2) &= rw \end{aligned} \right\} \text{when } w > 0 \quad (15)$$

and

$$\left. \begin{aligned} \frac{d}{dr}(ru_1) &= -\frac{1}{h_1}rw \\ \frac{d}{dr}(h_1ru_1 + h_2ru_2) &= 0 \end{aligned} \right\} \text{when } w < 0, \quad (16)$$

respectively. Similarly, the equations of absolute angular momentum are written as

$$\left. \begin{aligned} \frac{d}{dr}(ru_1M_1) &= -EM_1wr \\ \frac{d}{dr}(h_1ru_1M_1 + h_2ru_2M_2) &= mwr \end{aligned} \right\} \text{when } w > 0 \quad (17)$$

where M_1 is constant and

$$\left. \begin{aligned} \frac{d}{dr}(ru_1M_1) &= -\frac{1}{h_1}M_2wr \\ \frac{d}{dr}(h_1ru_1M_1 + h_2ru_2M_2) &= 0 \end{aligned} \right\} \text{when } w < 0 \quad (18)$$

where M_2 is constant.

Radial Mass Flux and Radial Velocity

Since the equations of continuity (15) and (16) are "exact", these equations can at once be integrated. Thus we have for the radial mass flux across the subsidence layer

$$h_1 r_R u_1 = -\sum_{n=1}^R \bar{w}_n (r_{n+1}^2 - r_n^2) \quad (19)$$

where \bar{w}_n is the modified vertical velocity given by

$$\bar{w}_n = \begin{cases} Eh_1 \bar{w}_n & \text{for updraft} \\ \bar{w}_n & \text{for downdraft} \end{cases} \quad (20)$$

in which \bar{w}_n is the mean vertical velocity between radii r_n and r_{n+1} .

Similarly, we have for the total mass flux across the outflow and the subsidence layers

$$h_1 r_1 u_1 + h_2 r_2 u_2 = \sum_{n=1}^R \bar{w}'_n (r_{n+1}^2 - r_n^2) \quad (21)$$

where \bar{w}'_n is given by

$$\bar{w}'_n = \begin{cases} \bar{w}_n & \text{for updraft} \\ 0 & \text{for downdraft} \end{cases} \quad (22)$$

Therefore, we have the radial velocities in the subsidence and the outflow layers

$$u_{1R} = -\frac{1}{r_1 h_1} \left[\sum_{n=1}^R \bar{w}_n (r_{n+1}^2 - r_n^2) \right] \quad (23)$$

$$u_{2R} = \frac{1}{r_2 h_2} \left[\sum_{n=1}^R \bar{w}'_n (r_{n+1}^2 - r_n^2) + \sum_{n=1}^R \bar{w}_n (r_{n+1}^2 - r_n^2) \right], \quad (24)$$

respectively.

Absolute Angular Momentum

Since M_1 is constant inside the updraft and M_2 is constant inside the downdraft, Eqs. (17) and (18) are "exact". Therefore, we have for the radial flux of absolute angular momentum across the subsidence layer

$$h_1 r_1 u_{1R} M_{1R} = - \sum_{n=1}^R \bar{w}_n \Omega_n (r_{n+1}^2 - r_n^2) \quad (25)$$

where Ω_n is the absolute angular momentum defined as

$$\Omega_n = \begin{cases} M_{1n-1} & \text{for updraft} \\ M_{2n-1} & \text{for downdraft} \end{cases} \quad (26)$$

Similarly we have for the total flux of the absolute angular momentum across the outflow and the subsidence layers

$$h_1 r_1 u_{1R} M_{1R} + h_2 r_2 u_{2R} M_{2R} = \sum_{n=1}^R \bar{w}'_n \bar{m}_n (r_{n+1}^2 - r_n^2) \quad (27)$$

where \bar{m}_n is the mean absolute angular momentum of radar echoes. We, therefore, have for the absolute angular momentum in the subsidence and the outflow layers

$$M_{1R} = - \frac{1}{h_1 r_R u_{1R}} \left[\sum_{n=1}^R \bar{w}_n \Omega_n (r_{n+1}^2 - r_n^2) \right] \quad (28)$$

and

$$M_{2R} = \frac{1}{h_2 r_R u_{2R}} \left[\sum_{n=1}^R \bar{w}'_n \bar{m}_n (r_{n+1}^2 - r_n^2) + \sum_{n=1}^R \bar{w}_n \Omega_n (r_{n+1}^2 - r_n^2) \right], \quad (29)$$

respectively, where \bar{w}_n , \bar{w}'_n , and Ω_n are given by Eqs. (20), (22), and (26), respectively.

Boundary Conditions and Other Conditions Required

In order to compute the continuity equations, (Eqs. (23) and (24)), and the equations of absolute angular momentum, Eqs. (28) and (29), the following boundary conditions were used:

For the radial velocity

$$u_{1E} = u_{2E} = 0 \quad (30)$$

where u_{1E} and u_{2E} are the radial velocities at the eye wall at the subsidence and the outflow layers, respectively.

For the absolute angular momentum

$$M_{1E} = M_{2E} = m_E \quad (31)$$

where M_{1E} and M_{2E} are the absolute angular momenta at the eye wall at the subsidence and the outflow layers, respectively, and m_E is the absolute angular momentum of the radar echo at the eye wall.

From Eq. (20) it is found that the radial velocity over the region of the inner rainbands is negative no matter how small the entrainment rate, and for a large value of entrainment the radial velocity over the region of outer rainbands could be negative even though the radial velocity over the region of the inner rainbands is not negative. Therefore, for the first run, when negative values of radial velocity appeared over the region of the updraft, they were replaced by zero where the absolute angular momentum remains constant by Eq. (13).

5. Computation of Three-Dimensional Wind and Pressure Fields

From the radial velocities and the angular momenta obtained above, the tangential and total velocities and the wind shears are computed. By using the equation of motion the pressure fields are obtained.

Tangential Velocity, Crossing Angle and Total Wind Velocity

The tangential velocity v_i , the crossing angle α_i , measured clockwise from the direction of the tangential wind, and the total wind velocity V_i are expressed by

$$\begin{aligned} v_i &= (M_i - \frac{1}{2} fr^2)r^{-1} \\ \alpha_i &= \tan^{-1} u_i / v_i \\ V_i &= \sqrt{u_i^2 + v_i^2} \end{aligned} \quad (32)$$

respectively.

Vertical Wind Shear

The wind shear between the outflow and the middle layers is given by

$$\delta V_{20} = \sqrt{(V_2 \sin \alpha_2)^2 + (V_2 \cos \alpha_2 - V_0)^2} \quad (33)$$

and

$$A_2 = \alpha_2 + \sin^{-1}(\sin \alpha_2 V_0 / \delta V_{20}) \quad (34)$$

where δV_{20} and A_{20} are respectively the magnitude and the crossing angle of the wind shear.

Similarly, the magnitude δV_{21} and the crossing angle A_{21} of the wind shear between the outflow and the subsidence layers are expressed as

$$\delta V_{21} = \sqrt{(V_2 \sin \alpha_2 - V_1 \sin \alpha_1)^2 + (V_2 \cos \alpha_2 - V_1 \cos \alpha_1)^2} \quad (35)$$

and

$$A_{21} = \alpha_2 + \sin^{-1}[\sin(\alpha_2 - \alpha_1) \cdot V_1 / \delta V_{21}] \quad (36)$$

When the absolute angular momentum remains constant inside the downdraft, $V_2 \cos \alpha_2 = V_1 \cos \alpha_1$, and, therefore, δV_{2l} can be reduced to

$$\delta V_{2l} = V_2 \sin \alpha_2 - V_1 \sin \alpha_1 \quad (37)$$

In this case, since $V_1 \sin(\alpha_2 - \alpha_1) / \delta V_{2l} = \cos \alpha_2$, the crossing angle A_{2l} becomes

$$A_{2l} = \alpha_2 + \frac{\pi}{2} - \alpha_1 = \frac{\pi}{2} \quad (38)$$

Pressure Field

For a steady state the equation of motion is

$$u_i \frac{\partial u_i}{\partial r} - u_i \frac{w}{h_i} - \left(\frac{v_i}{r} + f \right) v_i = - \frac{1}{\rho_i} \frac{\partial P_i}{\partial r}, \quad (39)$$

where P_i is the pressure and ρ_i the air density. This can also be written as

$$Z_i v_i + u_i \frac{w}{h_i} = - \frac{1}{\rho_i} \frac{\partial P_i}{\partial r} + \frac{1}{2} (u_i^2 + v_i^2) \quad (40)$$

where Z_i is the absolute vorticity and is given by

$$Z_i \equiv \frac{\partial v_i}{\partial r} + \frac{v_i}{r} + f. \quad (41)$$

Integrating Eq. (39) with respect to r , we have

$$P_{iR} = P_{ib} - \frac{1}{2} \rho_i (V_{iR}^2 - V_{ib}^2) - \rho_i \sum_{n=1}^R (Z_{in} v_{in} + u_{in} \frac{\bar{w}_n}{h_i}) \Delta r \quad (42)$$

where P_{ib} and V_{ib} are the pressure and the total wind velocity at the outer boundary, respectively, and Δr is the radial distance between r_n and r_{n+1} . The path of integration is taken toward the center from the outer boundary and the air density ρ_i assumed constant.

6. An Example of a Numerical Computation

In order to investigate the effect of entrainment on the outflow winds and the relation

between the orientation of the outflow cirrus and the vertical wind shear, two different runs were made with the same distribution of vertical velocity and absolute angular momentum of radar echoes. In the first run, when negative values of radial velocity appeared in the subsidence layer, they were replaced by zero. For the second run, the actual negative values were used. In this paper several results obtained from the first run are presented followed by some discussion of the results derived from the second run.

To obtain a finer structure of the typhoon outflow, the radius was divided into 10 km intervals. The thickness of the outflow and the subsidence layer was assumed to be constant, $h_1 = h_2 = 2$ km. Values up to 800 km from the storm center were computed by using the IBM 7094 computer at the University of Chicago. The distribution of vertical velocity used is presented in the figures. The radial distribution of absolute angular momentum of echoes is shown in Table 1 for every 100 km.

Table 1. Absolute Angular Momentum of Echoes

Radius	100	200	300	400	500	600	700	km
m	4.0	8.2	12.2	16.2	20.5	24.4	28.5	$\times 10^6 \text{ m}^2 \text{ sec}^{-1}$
$1/2 \text{ fr}^2$	0.4	1.5	3.3	5.8	9.1	13.1	17.9	$\times 10^6 \text{ m}^2 \text{ sec}^{-1}$
vr	3.6	6.7	8.9	10.4	11.4	11.3	10.6	$\times 10^6 \text{ m}^2 \text{ sec}^{-1}$

Wind Field

Figure 8 shows the distribution of the radial and the tangential velocities in the outflow layer for different entrainment rates. Since the radial velocity in the subsidence layer was replaced by zero when its value became negative the radial velocity is zero all over the region of the inner band in the subsidence layer and, therefore, no entrainment occurs into the inner rainband. Thus the radial and tangential velocities in the outflow layer take the same pattern over the inner rainband and the subsequent downdraft and the effect of entrainment appears only over the outer rainbands. When the entrainment rate is zero, the outflow winds obtained from the present model coincide with those obtained from the previous model.

As the entrainment rate increases the radial velocity increases and the negative value of tangential velocity also increases. This comes from the increase in the mass and the decrease in the absolute angular momentum due to the entrainment of the air in the subsidence layer into the updraft.

Presented in Fig. 9 is the distribution of the radial and the tangential velocities in the subsidence layer. For the reason mentioned above the radial velocity is zero all over the inner rainband and the radial velocities take the same pattern for different entrainment rates over the inner rainband and the subsequent downdraft. As the entrainment rate increases the radial velocity over the outer rainbands increases by entraining the air in the subsidence layer into the updraft and the negative value of tangential velocity increases since the absolute angular momentum in the subsidence layer is supplied only through the subsidence process from the outflow layer where the absolute angular momentum is decreasing through the process of entrainment.

Figures 10, 11, and 12 show the vertical cross section of the winds obtained from the present model. The wind pattern in the middle layer was obtained from the absolute angular momentum of the radar echoes which are shown in Table 1. Over the inner band and the subsequent downdraft the winds in the outflow and the subsidence layers take the same pattern for different entrainment rates. Over the outer rainbands, the wind direction changes clockwise in the outflow and the subsidence layers and the wind velocity increases in the outflow layer and decreases gradually in the subsidence layer. In the subsidence layer the cyclonic wind inside the inner rainband changes into the anticyclonic wind over the subsequent downdraft and then intensifies gradually toward the outer boundary as the entrainment rate increases.

Also presented in the figures are two different types of wind shear. The distribution of the wind shear between the outflow and the middle layers, indicated by longer arrows, takes the same pattern over the inner rainband and the subsequent downdraft for different entrainment rates since the wind pattern is the same. However, there is a slight increase in the speed of the wind shear when the entrainment rate increases, the crossing angle of the wind shear ranges from 160 to 180 degs. This direction of the wind shear ranging from 160 to 180 degs coincides with the general orientation of the wide bands of outer cirrus

bands as seen in the pictures which are shown in Figs. 1 through 5.

The radial distribution of the wind shear between the outflow and the subsidence layers for different entrainment rates is also indicated by shorter arrows in the pictures. Over the downdraft subsequent to the inner rainband the direction of the wind shear is exactly 90 degs as stated in the previous section. As the entrainment rate increases the direction of the wind shear approaches 90 degs over the downdraft in the region of the outer rainbands and beyond this region. This direction of the wind shear which is nearly 90 degs over the downdraft coincides with the direction of the transverse bands which are nearly perpendicular to the general orientation of the longitudinal bands of cirrus clouds as seen in the pictures which are shown in Figs. 1 through 5.

Pressure Field

Presented in Figs. 13 and 14 are the pressure profile at the outflow layer combined with two-dimensional distribution of the winds in the outflow and the middle layers and that of the wind shears between the outflow and the middle layers and between the outflow and the subsidence layers for two different entrainment rates. The pressure profile in the outflow layer was obtained from Eq. (42) by assuming that $P_{2b} = 200$ mb and $\rho_2 = 0.3430 \text{ kg m}^{-3}$. Following the path of integration used for Eq. (42), when viewed from the outer boundary of the storm, the pressure rises step-wise toward the center, each increase starting after the appearance of a rainband and each plateau corresponding to a region of downdraft. After reaching the highest level of pressure over the downdraft between the inner and the outer rainbands, the pressure falls rapidly near the eye of the storm. As the entrainment rate increases, this highest pressure gradually intensifies.

Additional Computations

The results discussed above were obtained under the assumption that the radial velocity in the subsidence layer is not negative. When negative values of the radial velocity appeared they were replaced by zero. In the second run this condition was eliminated. Some results thus obtained are as follows: (1) cyclonic winds blowing toward the storm center with some crossing angle are seen in the subsidence layer. This inward crossing angle becomes larger as the entrainment rate increases. (2) Since the radial velocity near the eye of the storm is so large, for a large entrainment rate, entrainment into the inner

rainband greatly affects the winds over and beyond the outer rainbands in the subsidence layer. (3) The value of the highest pressure over the downdraft subsequent to the inner rainband becomes much larger than that obtained from the first run when the entrainment rate increases.

7. Conclusions

From the Nimbus and ESSA pictures of hurricanes and typhoons it was found that longitudinal bands of outer convective clouds often are accompanied by well-defined transverse bands which are nearly perpendicular to the general pattern of these outer bands. In order to discuss this problem by generalizing the previous model of typhoons accompanied by inner and outer rainbands, the present model of typhoons with outflow and subsidence layers was proposed where entrainment of the air into the rainbands is taken into consideration.

When the entrainment rate is zero both the radial velocity and the absolute angular momentum in the outflow layer increase by receiving the mass and the absolute angular momentum of echoes supplied from the middle layer over the region of updraft while the radial velocity decreases by the subsidence process and the absolute angular momentum remains unchanged over the region of downdraft. Therefore, the wind pattern in the outflow layer obtained from the present model coincides with that obtained from the previous model. In the subsidence layer both the radial velocity and the absolute angular momentum increase over the region of downdraft while the radial velocity decreases and the absolute angular momentum remains unchanged over the region of updraft.

When entrainment occurs the equation of continuity requires inflow into the inner rainband in the subsidence layer. For the first run, when negative values of radial velocity appeared in the subsidence layer, they were replaced by zero. Therefore, no entrainment occurs into the inner rainband and actual entrainment appears over the outer rainbands in the subsidence layer where the decrease in the radial velocity becomes larger but the absolute angular momentum remains unchanged when the entrainment rate increases. Over the region of downdraft both the radial velocity and the absolute angular momentum increase in the subsidence layer. On the other hand, in the outflow layer both the radial velocity and the absolute angular momentum decrease over the region of downdraft while the radial

velocity increases and the absolute angular momentum decreases over the region of the outer rainbands.

From the computation of the pressure field it was found that the pressure in the outflow layer rises toward the center from the outer boundary, reaches the maximum value over the downdraft between the inner and the outer rainbands, then falls rapidly near the eye of the storm. This maximum value of pressure becomes larger as the entrainment rate increases.

One of the interesting results obtained from the present model is the relation of the general orientation of longitudinal bands and the direction of transverse bands as seen in satellite pictures, to the computed wind shear. The general orientation of the longitudinal bands coincides with the computed wind shear between the outflow and the middle layers, while the direction of the transverse bands coincides with the computed wind shear between the outflow and subsidence layers.

Acknowledgements:

The author is very grateful to Prof. Tetsuya T. Fujita for his many valuable suggestions and comments. Gratitude is also expressed to Mrs. Chieko Yata and Mr. Keiichi Nator, Meteorological Research Institute, Tokyo, Japan for their assistance in gridding the APT pictures presented in this paper.



REFERENCES

- Allison, L., G. Nicholas and J. Kennedy, 1966: Examples of the meteorological capability of the high resolution infrared radiometer on the Nimbus 1 satellite. J. Appl. Meteor., 5, No. 3, pp. 314-333.
- Chandra, K., 1938: Instability of fluids heated from below. Proc. Roy. Soc., A164, pp. 231-241.
- Fett, R., 1964: Aspects of hurricane structure: new model considerations suggested by TIROS and Project Mercury observations. Mo. Wea. Review, 92, No. 2, pp. 43-60.
- Fujita, T., T. Izawa, K. Watanabe and I. Imai, 1967: A model of typhoons accompanied by inner and outer rainbands. J. Appl. Meteor., 6, No. 1, pp. 3-19.
- Kuettner, J., 1959: The band structure of the atmosphere. Tellus, 11, pp. 267-294.
- Reap, R., 1966: Preliminary investigation of peripheral subsidence associated with hurricane outflow. SMRP Research Paper No. 63, 19 pp.
- Tsuchiya, K. and T. Fujita, 1967: A satellite meteorological study of evaporation and cloud formation over the Western Pacific under the influence of the Winter Monsoon. J. Meteor. Soc. Japan, Ser. II, 45, No. 3, pp. 232-250.

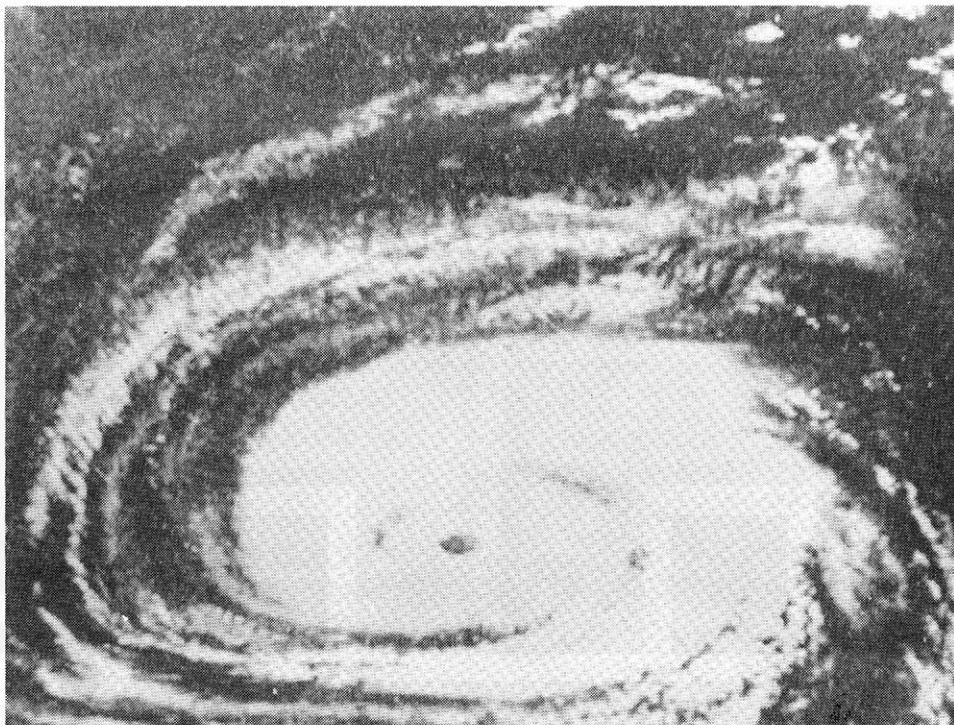


Fig. 1. An HRIR photofacsimile depiction of Hurricane Gladys taken on Orbit.305 at 0422 U T., 18 September 1964. To the west and north of the storm may be seen well-defined longitudinal and transverse bands of clouds.

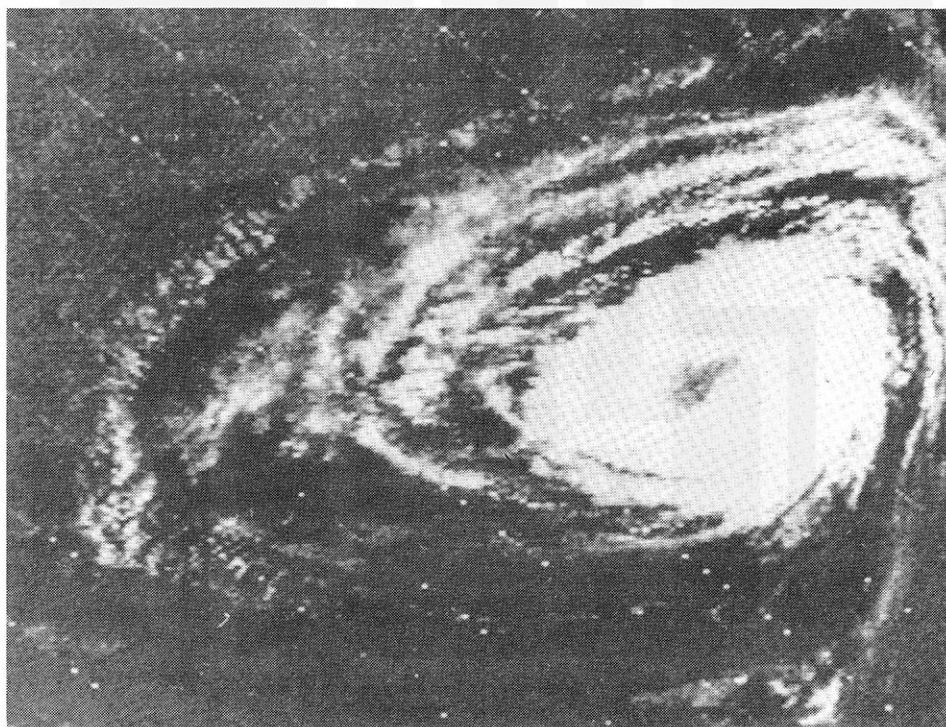


Fig. 2. An enlarged HRIR photofacsimile depiction of Hurricane Dora taken on Orbit 174 at 0530 U.T., 9 September 1964. In the northwest quadrant may be seen longitudinal bands of outer convective clouds accompanied by well-defined transverse bands.

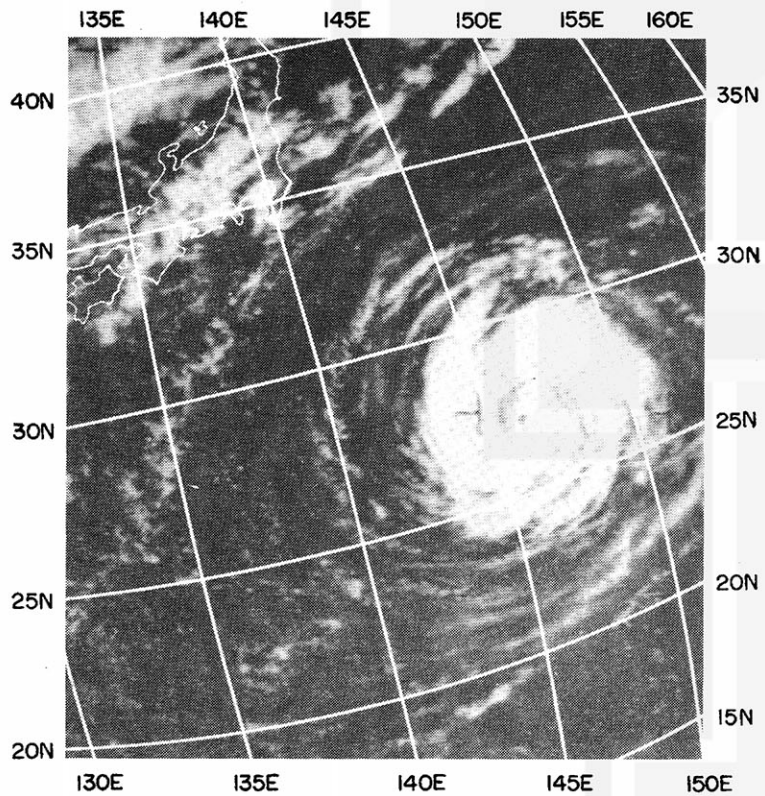


Fig. 3. An ESSA-2 APT picture of Typhoon Opal taken on Orbit 7052 at 2228Z, 8 September 1967. Around the storm may be seen longitudinal bands of outer convective clouds accompanied by marked transverse bands.

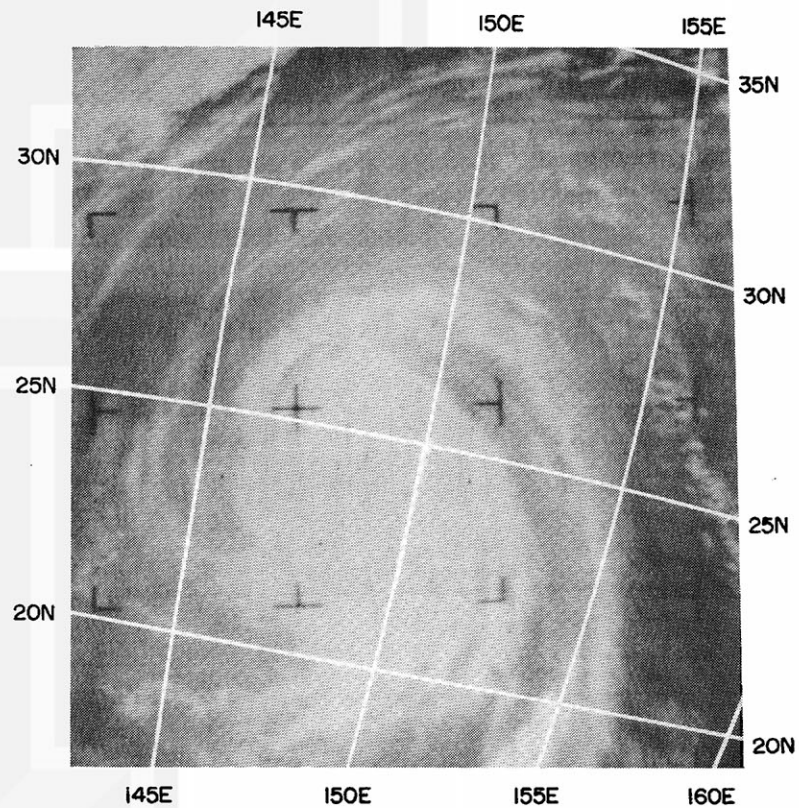


Fig. 4. A Nimbus-2 APT picture of Typhoon Amy taken on Orbit 6747 at 0153Z, 4 October 1967. To the east of the storm may be seen longitudinal bands of outer convective clouds accompanied by transverse bands.

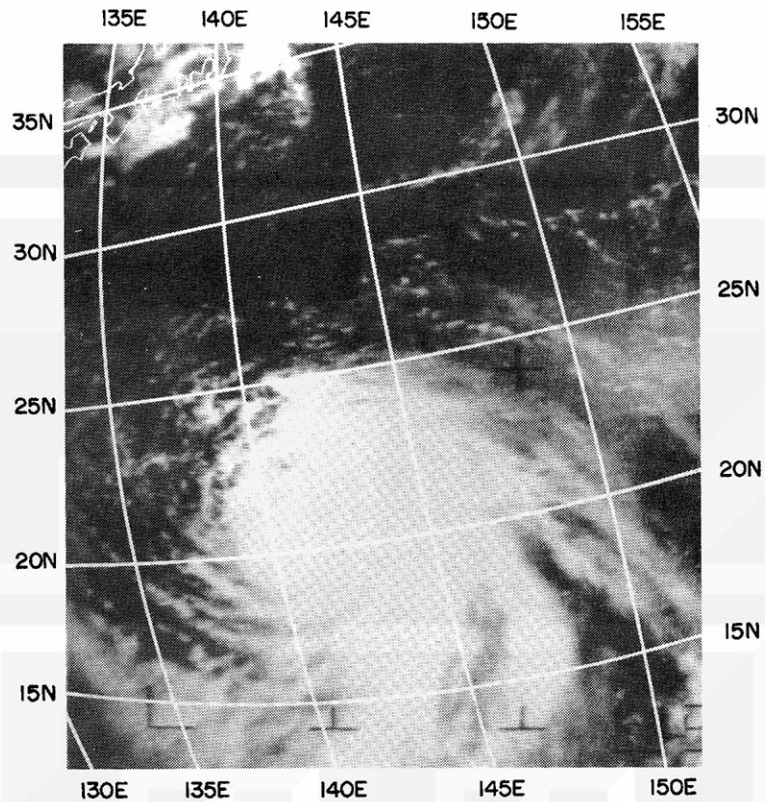


Fig. 5. An ESSA-6 APT picture of Typhoon Mary taken on Orbit 3212 at 0018Z, 24 July 1968. To the west of the storm may be seen ill-defined transverse bands which are nearly perpendicular to longitudinal bands of outer convective clouds.

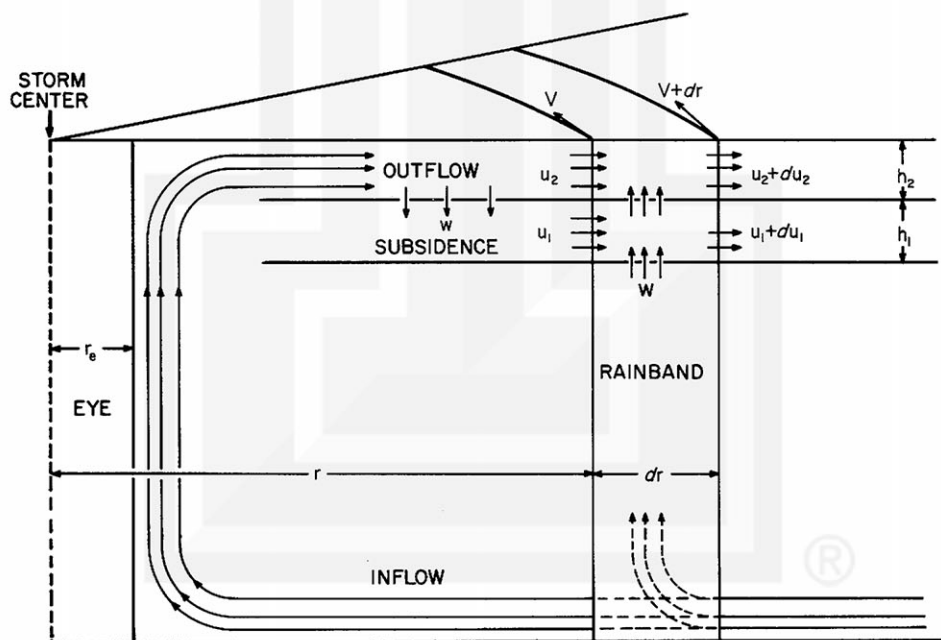


Fig. 6. Schematic model of typhoon with outflow and subsidence layers.

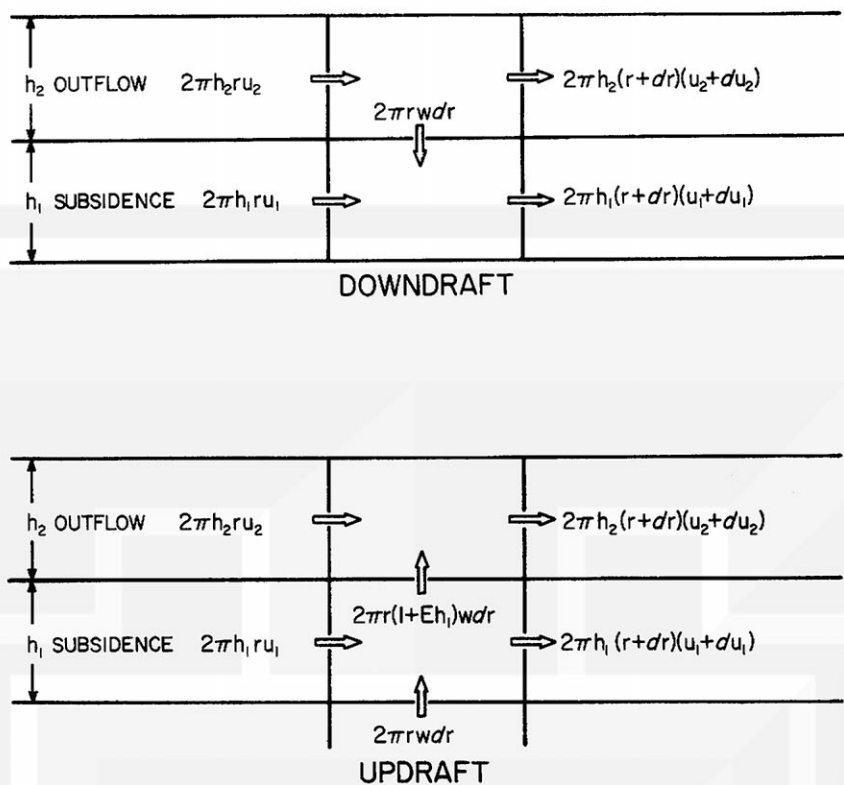


Fig. 7. Radial and vertical mass flux for the regions of downdraft and updraft.

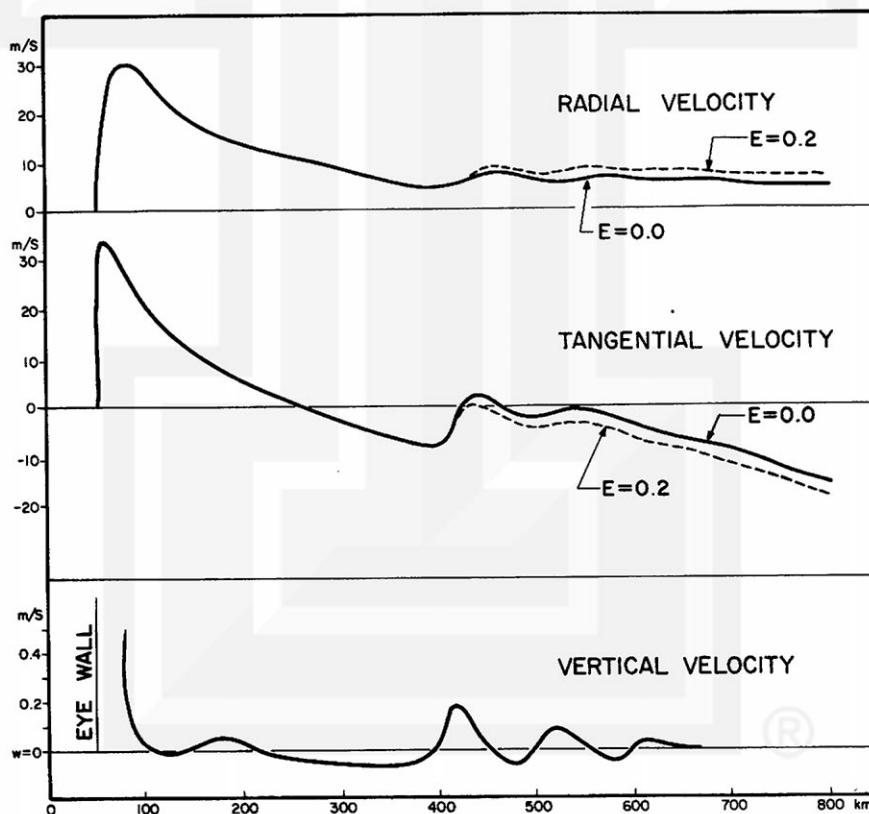


Fig. 8. Distribution of radial and tangential velocities at the outflow layer for different entrainment rates.

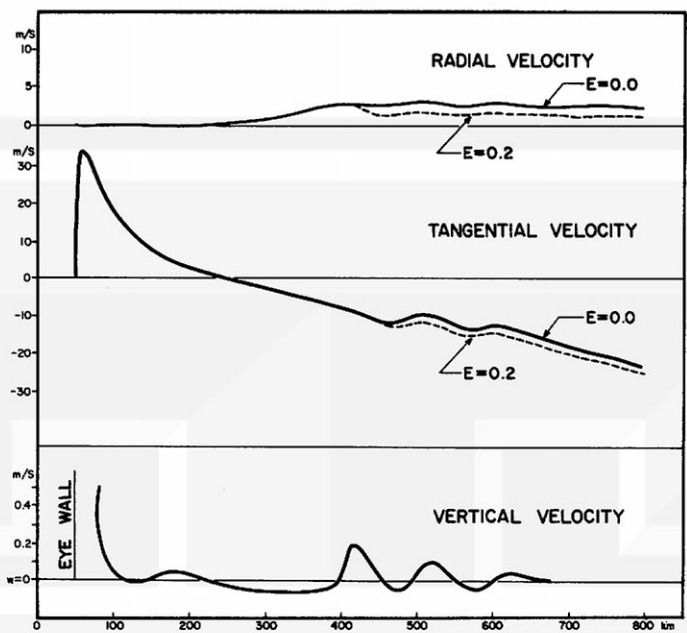


Fig. 9. Distribution of radial and tangential velocities at the subsidence layer for different entrainment rates.

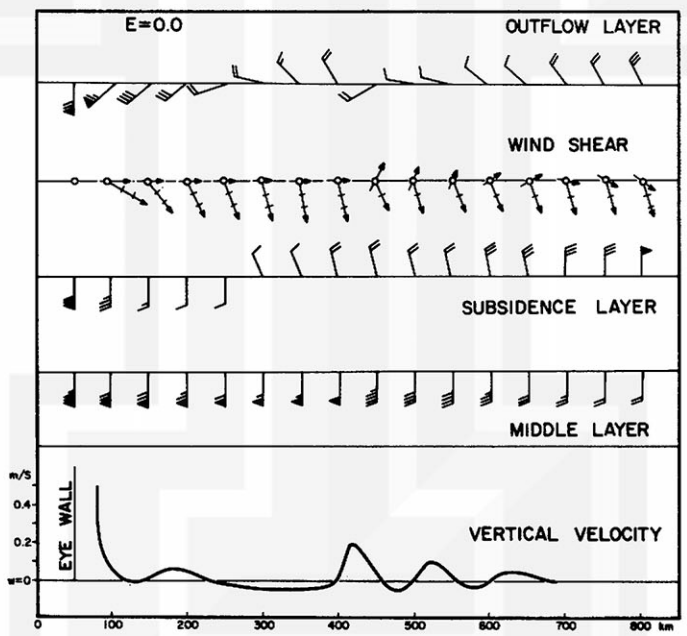


Fig. 10. Vertical cross section of winds in knots combined with two different types of wind shear when the entrainment rate E is zero. The wind shear between the outflow and the middle layers is indicated by longer arrows radiating from the circle, graduated in 10 knots. The wind shear between the outflow and the subsidence layers is indicated by shorter arrows across the circle with the same scale.

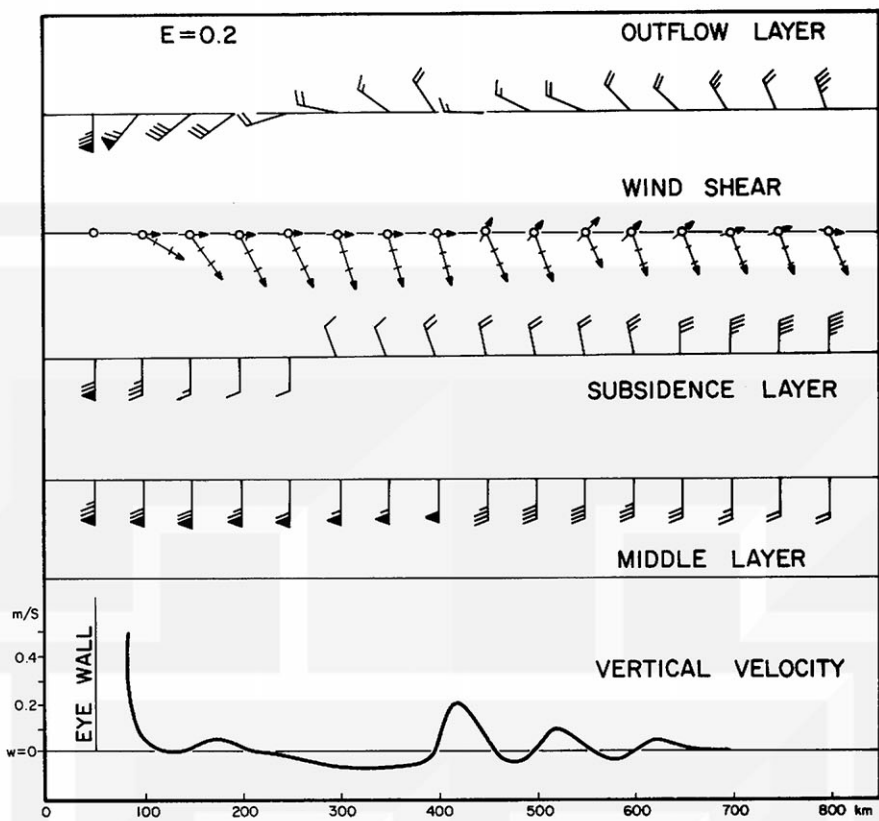


Fig. 11. Same as Fig. 10 except the entrainment rate E is 0.2.

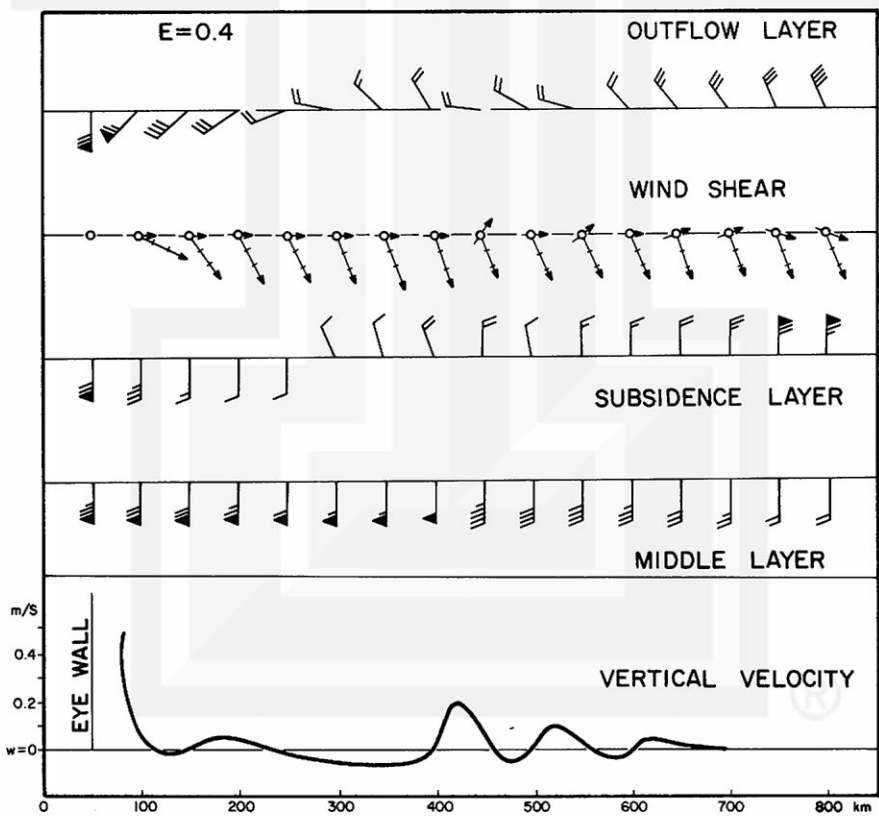


Fig. 12. Same as Fig. 10 except the entrainment rate E is 0.4.

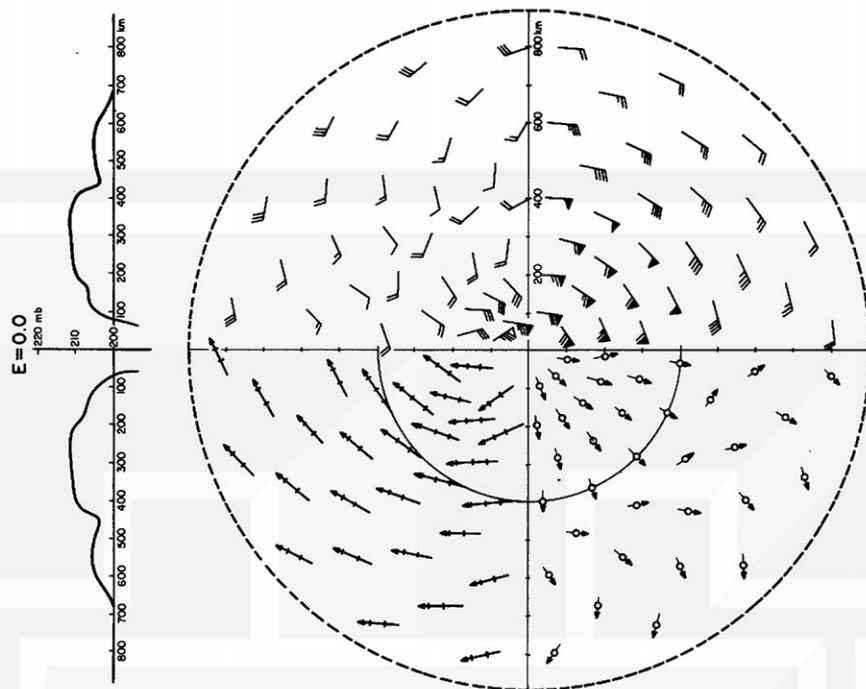


Fig. 13. Pressure profile at the outflow layer combined with a two-dimensional distribution of winds for different layers and of different types of wind shear when the entrainment rate is zero. Presented at the upper left and right quadrants are the horizontal wind distributions for the outflow and the middle layers, respectively. The wind shear between the outflow and subsidence layers is shown at the lower left quadrant while the wind shear between the outflow and the middle layers is shown at the lower right quadrant.

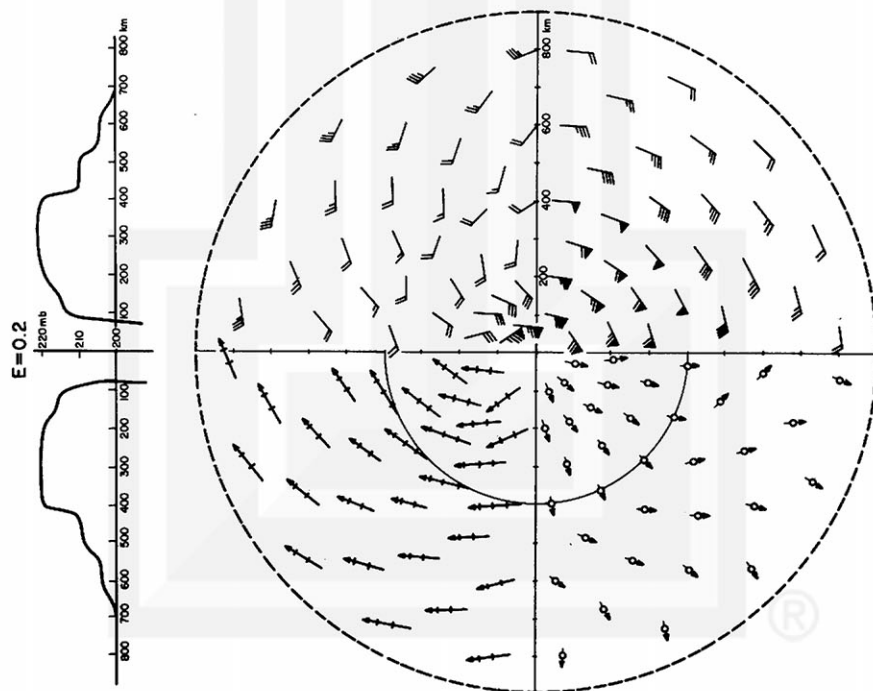


Fig. 14. Same as Fig. 13 except the entrainment rate E is 0.2.

MESOMETEOROLOGY PROJECT - - - RESEARCH PAPERS

(Continued from front cover)

42. * A Study of Factors Contributing to Dissipation of Energy in a Developing Cumulonimbus - Rodger A. Brown and Tetsuya Fujita
43. A Program for Computer Gridding of Satellite Photographs for Mesoscale Research - William D. Bonner
44. Comparison of Grassland Surface Temperatures Measured by TIROS VII and Airborne Radiometers under Clear Sky and Cirriform Cloud Conditions - Ronald M. Reap
45. Death Valley Temperature Analysis Utilizing Nimbus I Infrared Data and Ground-Based Measurements - Ronald M. Reap and Tetsuya Fujita
46. On the "Thunderstorm-High Controversy" - Rodger A. Brown
47. Application of Precise Fujita Method on Nimbus I Photo Gridding - Lt. Cmd. Ruben Nasta
48. A Proposed Method of Estimating Cloud-top Temperature, Cloud Cover, and Emissivity and Whiteness of Clouds from Short- and Long-wave Radiation Data Obtained by TIROS Scanning Radiometers - T. Fujita and H. Grandoso
49. Aerial Survey of the Palm Sunday Tornadoes of April 11, 1965 - Tetsuya Fujita
50. Early Stage of Tornado Development as Revealed by Satellite Photographs - Tetsuya Fujita
51. Features and Motions of Radar Echoes on Palm Sunday, 1965 - D. L. Bradbury and Tetsuya Fujita
52. Stability and Differential Advection Associated with Tornado Development - Tetsuya Fujita and Dorothy L. Bradbury
53. Estimated Wind Speeds of the Palm Sunday Tornadoes - Tetsuya Fujita
54. On the Determination of Exchange Coefficients: Part II - Rotating and Nonrotating Convective Currents - Rodger A. Brown
55. Satellite Meteorological Study of Evaporation and Cloud Formation over the Western Pacific under the Influence of the Winter Monsoon - K. Tsuchiya and T. Fujita
56. A Proposed Mechanism of Snowstorm Mesojet over Japan under the Influence of the Winter Monsoon - T. Fujita and K. Tsuchiya
57. Some Effects of Lake Michigan upon Squall Lines and Summertime Convection - Walter A. Lyons
58. Angular Dependence of Reflection from Stratiform Clouds as Measured by TIROS IV Scanning Radiometers - A. Rabbe
59. Use of Wet-beam Doppler Winds in the Determination of the Vertical Velocity of Raindrops inside Hurricane Rainbands - T. Fujita, P. Black and A. Loesch
60. A Model of Typhoons Accompanied by Inner and Outer Rainbands - Tetsuya Fujita, Tatsuo Izawa, Kazuo Watanabe, and Ichiro Imai

MESOMETEOROLOGY PROJECT - - - RESEARCH PAPERS

(Continued from inside back cover)

61. Three-Dimensional Growth Characteristics of an Orographic Thunderstorm System - Rodger A. Brown.
62. Split of a Thunderstorm into Anticyclonic and Cyclonic Storms and their Motion as Determined from Numerical Model Experiments - Tetsuya Fujita and Hector Grandoso.
63. Preliminary Investigation of Peripheral Subsidence Associated with Hurricane Outflow - Ronald M. Reap.
64. The Time Change of Cloud Features in Hurricane Anna, 1961, from the Easterly Wave Stage to Hurricane Dissipation - James E. Arnold.
65. Easterly Wave Activity over Africa and in the Atlantic with a Note on the Inter-tropical Convergence Zone during Early July 1961 - James E. Arnold.
66. Mesoscale Motions in Oceanic Stratus as Revealed by Satellite Data - Walter A. Lyons and Tetsuya Fujita.
67. Mesoscale Aspects of Orographic Influences on Flow and Precipitation Patterns - Tetsuya Fujita.
68. A Mesometeorological Study of a Subtropical Mesocyclone - Hidetoshi Arakawa, Kazuo Watanabe, Kiyoshi Tsuchiya, and Tetsuya Fujita.
69. Estimation of Tornado Wind Speed from Characteristic Ground Marks - Tetsuya Fujita, Dorothy L. Bradbury, and Peter G. Black.
70. Computation of Height and Velocity of Clouds from Dual, Whole-Sky, Time-Lapse Picture Sequences - Dorothy L. Bradbury and Tetsuya Fujita.
71. A Study of Mesoscale Cloud Motions Computed from ATS-I and Terrestrial Photographs - Tetsuya Fujita, Dorothy L. Bradbury, Clifford Murino, and Louis Hull.
72. Aerial Measurement of Radiation Temperatures over Mt. Fuji and Tokyo Areas and Their Application to the Determination of Ground- and Water-Surface Temperatures - Tetsuya Fujita, Gisela Baralt, and Kiyoshi Tsuchiya.
73. Angular Dependence of Reflected Solar Radiation from Sahara Measured by TIROS VII in a Torquing Maneuver - Rene Mendez.
74. The Control of Summertime Cumuli and Thunderstorms by Lake Michigan During Non-Lake Breeze Conditions - Walter A. Lyons and John W. Wilson.
75. Heavy Snow in the Chicago Area as Revealed by Satellite Pictures - James Bunting and Donna Lamb.